Sustainable Energy Project 2018

The Development and Production of Yet Another Wind Turbine

SEP Group 12

Jack Berg	s1537233
Robin Larsen Horn	s1468382
Amos Kennerley	s1555438
Craig Martin	s1441373
Nathan Whear	s1532760

The University of Edinburgh

April 6, 2018

Abstract

YAWT is a horizontal axis micro wind turbine, it weighs approximately 2.96kg, including the mass of two Samsung Galaxy Note 8 phones, and occupies about 1.8L (1.8×10^{-3})when packed. It uses control systems to manage the turbine to power ancillaries and charge multiple devices, presenting the user with an intuitive GUI, to relay information and customise settings. It also features smart safety systems to manage power levels and protect both the user and the device.

The machine is capable of producing an output voltage with an amplitude of 2V at 2000RPM. Which extrapolates to 4.96V DC at 3000RPM. However, the output contains a lot of harmonic distortion.

Contents

1 Introduction

1.1 Design Brief

All of the design decisions taken in developing the prototype of YAWT have been founded in the design specification laid out by the customer. The first criteria that needs to be met governed our design of the generator and the array of blades. The turbine must be capable of producing 10W of power to charge the users devices, plus any power needed for ancillary systems, we estimate this will be an additional 2.5W, at $12ms^{-1}$. The device should produce enough power at $8ms^{-1}$ to power all ancillary systems and begin to supply charge to the users device(s).

The customer has requested that we develop a generator that is optimised for this function. This was interpreted as an instruction to minimise the weight of the generator, whilst maximising the integrity of the design (it must be carried about in a backpack etc.).

The user should be shielded from any potentially dangerous moving parts, this primarily concerns the blades as other moving parts should be encased in the nacelle. This could take the form of a blade guard as seen in modern drone/quad-copter technology, this is TRL9 [8]. Alternatively, we could employ a larger shroud, this could act as a venturi allowing us to modify the flow past the blades, though this will dramatically influence the side profile of the turbine.

The customer has specified that the turbine should work in wet conditions, specifically all components should be IP67 rated as specified in the international standard EN 60529 [14]. We have interpreted this as all exposed components must be IP67 rated, otherwise any component must be enclosed in an IP67 environment. We are looking to include the users devices in the IP enclosure, as we feel they would reasonable expect to charge their devices in a safe location.

Finally the customer has a standardised mounting unit they wish this turbine to interface with, this should be incorporated. As a consideration for further development we could look to produce an adapter for other standard mounts, for example a camera tripod per ISO 1222:2010[2].

1.2 Comparable / Rival Systems

In our preliminary market research for comparable products we discovered a few rivals that also look to be targeting the outdoor enthusiast market. Firstly, there is WaterLily [29] who we believe to be the closest competitor with a market ready product. Their product is designed for operation in both wind and water, and as such produces less power than we aim to at our target wind speed. It has a diameter of 180mm and weighs only 1.3kg. Nils Ferber [11] has developed a collapsible Savonius turbine capable of operating at $5ms^{-1}$ and producing 5W of power, it weighs approximately 1.8kg. Our specification suggests operating at a much higher wind speed, where a horizontal axis machine may be advantageous.

2 Generator Design

2.1 Design Criteria

As the weight of the wind turbine had to be kept to a minimum, a custom lightweight generator was designed. The performance of the generator was simulated using EMS; an FEM-based electromagnetic simulation software provided by EMWorks. Several iterations of design and simulation were performed before a prototype was produced, and selected results from the final simulation are included below. The weight achieved for the prototype was 134.9g.

The generator was designed to supply two USB chargers rated at 1A, and a microprocessor unit. The MCU was used to control the rotor speed of the turbine and to monitor the temperature of the system. For the prototype,

(a) Render of the generator

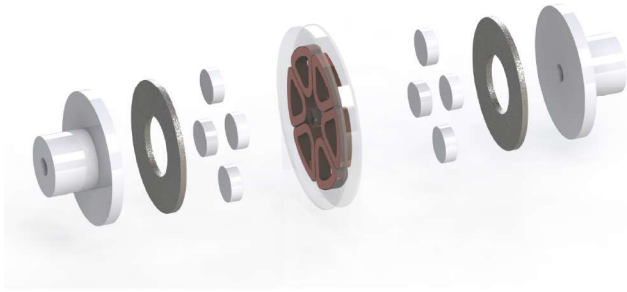

(b) Render of generator in an exploded view.

Figure 1

an Arduino Uno was used for this purpose. However, to reduce the power demand and the weight of the system, a more customised solution should be developed for the final product. The Arduino was powered by an internal USB port, and was estimated to draw a maximum of 500mA. As the USB ports operate at 5V, the required power was calculated as:

$$P = 5 \times 2.5 = 12.5W$$

To offset potential losses, the generator was designed to output 15W.

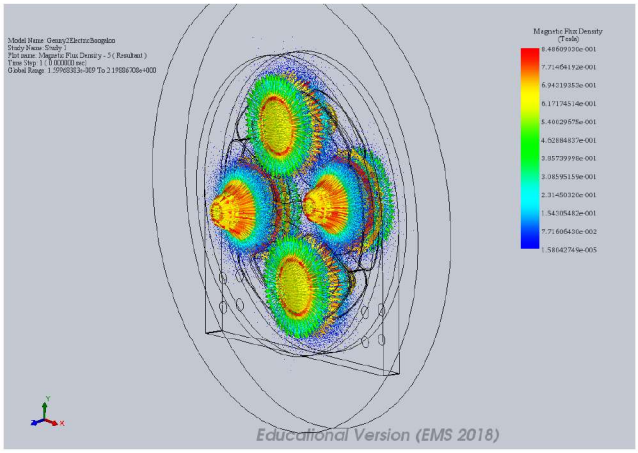

(a) FEA Study of the Flux Flow Through the Stator.

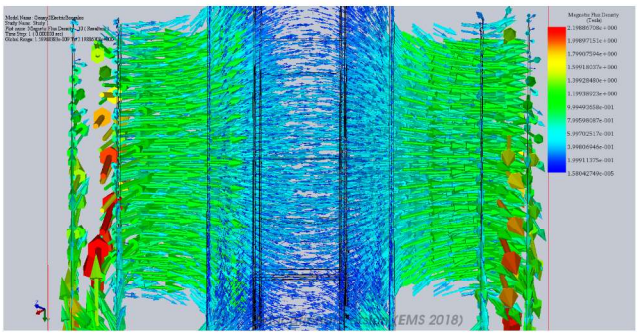

(b) FEA Study of the Flux Flow Through the airgap

Figure 2

2.2 Design

An axial flux design was chosen for the generator. This decision was largely based on the ease of manufacture considering the equipment available. The suggested design consists of a stator containing the armature windings, and one rotor on each side of the stator. To provide the magnetic flux, each rotor will be fitted with rare earth magnets fixed to a mild steel plate. These back-irons give the flux a low reluctance path along the pole pairs, and as they rotate at the same speed as the magnets there will be no associated iron losses. As can be seen in figure 2b, the flux vectors have small radial components when crossing the armature windings. Thus, eliminating the need

for stator cores. A coreless design significantly reduces the weight of the machine, making it highly suitable for a portable wind turbine. It also increases the overall efficiency as the machine produces no iron losses. The proposed design does require more PM material than similar iron-cored machines, but this disadvantage was considered minor at this scale, and was offset by the low weight achievable with a coreless construction. Finally, the axial design allowed the airgap length to be easily adjusted. The length of the airgap is inversely related to the power output of the generator, which makes this a very useful feature for the prototype. The generator was simulated with an airgap of 8mm.

The frequency of the generator output is a function of its rotational speed and number of pole pairs. However, in this application, the frequency is irrelevant as the output is rectified. Hence, the number of pole pairs can be optimised for other criteria instead. The permanent magnets are the most expensive components of the generator. As such the machine was designed to use as few magnets as possible. This measure also helped reduce the weight even further. To ensure that the machine had an integer number of pole pairs, the number of magnets had to be even. A two-pole design would make it more difficult to balance the rotors, potentially causing unacceptably large vibrations in the system. Therefore, the generator was designed to have four magnetic poles per rotor. In a further effort to minimise the cost and weight of the generator, it was decided to use small, standard-sized magnets. Several iterations of 3D-FEM analysis were performed until a satisfactory balance between size, weight, cost and strength could be found. Ultimately, 12x4 mm circular N42 magnets were chosen as they were the smallest magnets available from the university suppliers that could produce a sufficient flux density in the airgap.

To minimise the harmonic content of the generator output, the shape of the coils had to be optimised for the selected magnets. For the voltage induced in the coils to behave sinusoidally, the span of the coils must not be so high that one coil faces two coils of the same orientation. If this happens, the voltage induced in one side of the coil would be cancelled out by the voltage induced in the other side causing harmonic distortion to the output. For the same reason, the coil span can not be so low that one magnet faces both sides of the same coil. For a generator of this size, a design with one coil per phase would require the coils to be shaped like arc segments, while two coils per phase would cause the coils to be shaped like triangles. As triangular coils would be easier to produce with the available equipment, the machine was designed to have two coils per phase. The length of the airgap was minimised by embedding the coils in the stator and sealing them in with epoxy.

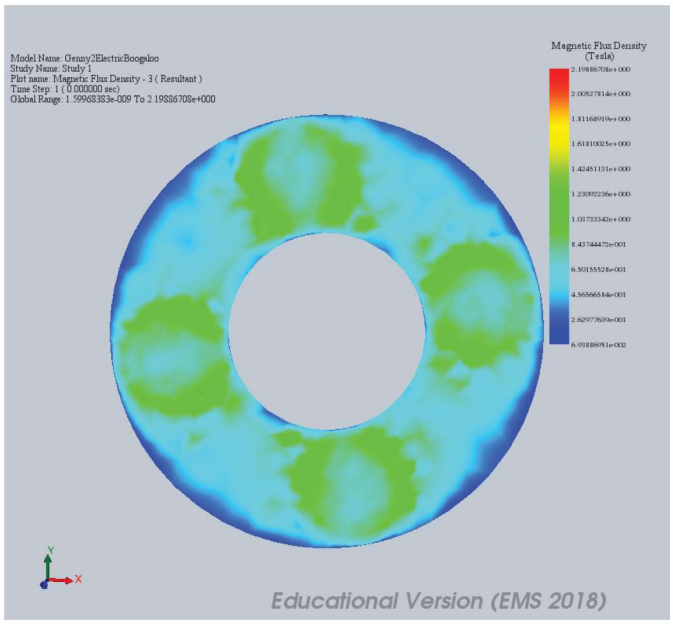

Figure 3: Flux Density in the Rotor Back-Iron.

To allow a reasonable clearance between the drive shaft and the coils, the inner diameter of the back-iron was set to 20 mm. The outer diameter was then set to 44 mm to allow room for the magnets. Its thickness was decided by simulating the flux flow through the rotor back-irons using EMS. The plates had to be as thin as possible to reduce the weight, but thick enough to avoid magnetic saturation. Furthermore, a standard thickness had to be chosen to

reduce costs. A thickness of 2 mm was found to be the thinnest standard size to avoid saturation, and the resulting flux density can be seen in figure 3. The voltage induced in one phase of armature winding was calculated as [1]:

$$v_{ph} = 0.029 \times T_{ph} \times B_{ag} \times N_{rpm} \times D_O^2 \left(1 - \left(\frac{D_i}{D_o}\right)^2\right)$$

Where: T_ph is the number of turns per phase, B_{ag} is the average flux density, N_{rpm} is the speed of the generator, D_i and D_o are inner/outer diameters of the back-iron.

Assuming the flux density in the airgap is sinusoidal, the average flux can be expressed as:

$$B_{ag} = \frac{1}{\pi}\int_0^{\pi} B_m \sin(\omega t) d(\omega t) = \frac{2B_m}{\pi}$$

Looking at figure 2b, the peak flux density in middle of the airgap is approximately 0.50 T. So, the average flux density is calculated to be:

$$B_{ag} = \frac{2B_m}{\pi} = \frac{2 * 0.5}{\pi} \approx 0.32T$$

As the USB ports operate at 5 V DC, the output phase voltage of the generator must be $\frac{V_{dc}\pi}{3\sqrt{3}} = \frac{5\pi}{3\sqrt{3}} = 3V$ at the optimal speed of the generator. However, to offset the voltage drop across the coils and other potential losses, the prototype will be designed for a phase voltage of 6 V. The equation below shows a rearrangement to find the required number of turns per phase.

$$T_{ph} = \frac{v_{ph}}{\left[0.029 B_{ag} N_{rpm} D_o^2 \left(1 - \left(\frac{D_i}{D_o}\right)^2\right)\right]} = \frac{6}{0.029 * 0.32 * 3000 * 0.044^2 \left(1 - \frac{0.020^2}{0.044^2}\right) = 141.5}$$

Hence, the number of turns per phase is chosen to be 142. However, due to the small size of the proposed design and the high safety factor applied when determining the number of turns per phase, it proved difficult to achieve a sufficiently wide coil span. Some harmonic distortion is therefore expected for the prototype, but is likely to be reduced or removed in future iterations of the design.

For the prototype, the maximum permissible current density per phase was estimated as $5Amm^{-2}$ Assuming that the maximum current flowing through one phase is, $I_ph = \frac{1}{3}\frac{15W}{5V} = 1A$, the minimum wire gauge was calculated as: $d_w = \sqrt{\frac{I_ph}{5\pi}} \approx 0.25mm$

However, as overloading the wires could damage the equipment and potentially cause a fire, a safety factor of 2 was applied to the prototype. Hence, Ø0.5 mm wire was chosen for the coils. The maximum fill factor for this diameter of wire is 90% [16]; however, as the coils would be wound by hand, the achievable fill factor for the prototype was estimated to be less than 85%. The designed coils had a cross-sectional area of $3.4x5mm^2$, giving a fill factor of: $\frac{0.25^2\pi * 71}{3.4 * 5} * 100\% \approx 82\%$ For future iterations of the generator, the possibility of reducing the wire gauge should be investigated, and the fill factor should be increased. This will allow the coil span to be increased, which will reduce the harmonic content of the output and increase the power quality of the wind turbine.

2.3 Results and Analysis

The generator was tested by securing the stator in a vice and driving the rotors with a pillar drill, while a Hantek 6022BE digital oscilloscope was used to measure the output phase voltage. It was found that an airgap length of 6 mm was achievable, but to achieve a meaningful comparison between test results and the data derived from the simulations, the generator was tested with an airgap length of 8 mm. Although, the airgap should be made as short as possible for the final design. Due to the operational limits of the drill, the generator could not be tested at its optimal speed. However, as the induced voltage is linearly related to the speed of the generator, the induced voltage at 3000 rpm could be extrapolated from the results optained at 2000 rpm. The test result are shown in figure 4. The peak voltage is about 2 V at 2000 rpm. So, the generator will output $2\frac{3000}{2000} = 3V$ at the designed speed. While, this is exactly the output voltage required by the generator, it is only 50% of the designed value. Therefore, the cause of the high losses should be investigated to increase the efficiency of the next iteration of the design. Due

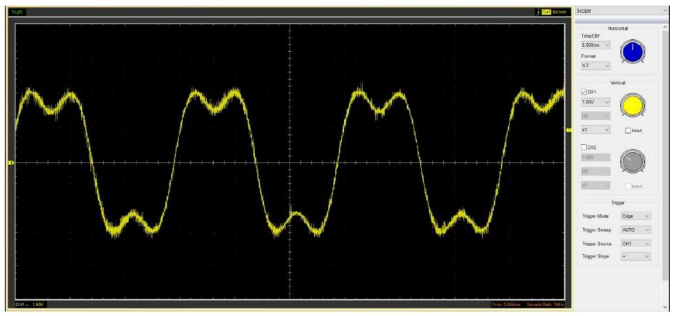

Figure 4: Measured Phase Voltage Output

to the high impedance of the oscilloscope, it can be assumed that the voltage drop across the armature winding is negligible. Instead, the losses can be explained by the high harmonic content present in the output. The fill factor achieved by hand winding the coils was only 56%; significantly lower than anticipated. As a result, the coil span had to be reduced well below the acceptable limit, which is likely the cause of the distortion.

2.4 Further Development

To improve the power quality of future designs, steps should be taken to reduce the harmonic distortion. It is expected that the coil span can be increased to an acceptable level by reducing the wire diameter to 0.4 mm and using automated machinery to increase the fill factor of the coils. If the losses are reduced, fewer turns per phase will be needed, and the efficiency can be increased further. The rotors used for the prototype were 3D printed, but to reduce costs, injection moulding should be considered for the final product. Similarly, the back-irons were laser cut for the prototype, but could be stamped if the product was to be mass-produced. The back-iron and magnets were epoxied to the rotor. Due to the high operational speed expected, the rotors were fixed to the shaft using grub screws and two brass Heat-Sert inserts situated at 120 deg to each other. However, once a final airgap length is settled upon, the cost of the product can be reduced by fixing the rotors to the shaft using spring pins. Finally, the stator for the prototype was laser cut from acrylic, but similarly to the rotors, it can be produced by injection moulding.

3 Blade Design

3.1 Aerofoil Selection

The first step in the blade design process was to select the aerofoil or aerofoils to be used. There were a number of key requirements to fulfil when selecting the aerofoil, the primary of which was the thickness. The aerofoil was required to be thick enough at all points in every element to ensure that it could be manufactured. This thickness also ensured it was strong enough to withstand the loads applied during operation and was robust enough to be transported without damage.

In the design of larger turbines, multiple aerofoil profiles are used along the length of the blade. This is to achieve a thicker structural base while still having a very efficient, high lift over drag profile at the tip. An intermediate profile is normally used for the centre section of the blade that compromises between thickness and efficiency. For smaller scale turbines, it is much simpler to use one profile for the full blade. This ensures the blade is smooth along the full length and the profiles do not require blending. This is possible since the blade is not required to support the same mass as it is far shorter.

The secondary requirements were a high lift coefficient and a high lift over drag value. It was also preferable for the aerofoil used to have a wide range of angles of attack for which it generates lift. Another desirable characteristic for the aerofoil to have smooth and predictable relationship between angle of attack and lift coefficient.

3.2 Blade Design Procedure

The first step in the blade design procedure was to determine the inner and outer radius of the blades. This was done by estimating the power coefficient of the blades with a conservative estimate and then substituting this into the wind power equation below

$$P = \frac{\rho C_p A V^3}{2}$$

The inner radius of the blades was determined by investigating the minimum area required for a shaft, hub and blade attachment method, or the manufacture method used. In this case the maximum blade length was defined by the 3D printer used. This constrained the length of the blades to a maximum of 150mm. For analysis, the blade is divided into a number of elements, in this case 50, along its length. These elements are then analysed individually and are then lofted between to produce the final blade profile.

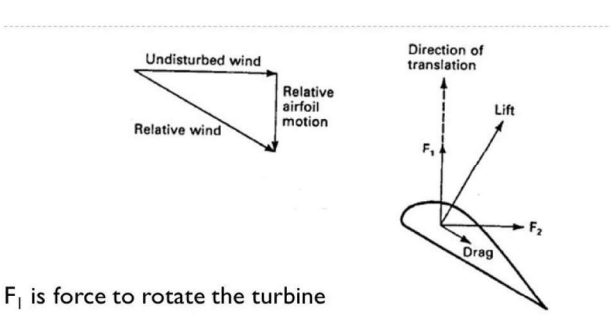

(a) Relative wind resolution graph

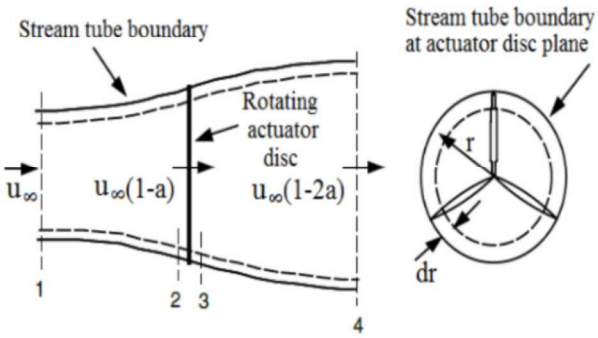

(b) Geometry for rotor analysis

Figure 5

The second step in designing the blades is to determine the relative wind direction. The primary difficulty is accounting for the pressure increase, and therefore velocity decrease, in the wind before reaching the blade surface. This pressure change can be seen in figure 5b below which shows the stream boundaries as the air passes through the rotor. In the method used to design the blades, the initial assumption is that the velocity reduction will be optimal, therefore the axial induction factor will be assumed to be $\frac{1}{3}$. Thus, at the operating free stream wind speed of $12ms^{-1}$, the wind speed at the blade surface will be initially assumed to be $8ms^{-1}$.
Following this the operating rpm of the turbine was then determined. The main factors effecting the chosen RPM of the blades was the generator's operating range. This was found by experimentation to be a minimum of 3000rpm. This is to ensure an appropriate voltage is produced to charge the devices. Another significant factor is the efficiency of the blades at the chosen rpm and relative wind speed. At lower tip speed ratios the angular velocity imparted to the air over the blade length is significant and would need to be considered. Thus a high tip speed ratio is desired to allow wake rotation to be neglected in the analysis.

Following this, the perceived wind velocity and relative wind direction for each element can be determined using the equations below.

$$ApparentWindSpeed = \sqrt{\left(\frac{2}{3} \times WindSpeed\right)^2 + (BladeElementSpeed)^2}$$

$$WindAngle = \arctan\left(\frac{2 \times WindSpeed}{3 \times BladeSpeed}\right)$$

The tip loss factor for each blade element was calculated and the optimal angle for the aerofoil for each blade element was then determined using the relative wind direction and the attack angle selected earlier.The tip loss factor was then determined and then the chord length of the aerofoil at each element was then calculated.

$$F_i = (2/\pi)arccos[exp[\frac{(n/2)[(r_i/R) - 1]}{(r_i/R)sin(WindAngle)}]$$

[17]

$$C_i = \frac{8\pi r_i F_i sinWindAngle}{nC_l} \frac{cos(WindAngle) - speedRatio_i sin(WindAngle)}{(r_i/R_i)sin(WindAngle)}$$

[17]

Following the chord length being determined, the solidity at each radius is then calculated.

$$s_i = \frac{nC_l}{2\pi r}$$

The axial induction factor and angular induction factors were then calculated and compared to those assumed at the start of the process. If the new, calculated value and the original, assumed, value are outwith an acceptable level or error, then the new axial and angular induction factors are substituted into the original equation and the values are recomputed using the equations below. This is repeated until the factors converge.

$$a = \frac{1}{[1 + [4F_i sin^2(WindAngle)/(s_i C_l)cos(WindAngle)]]}$$

Finally the power coefficient of the blades was calculated and the final power output of the blades was determined and torque and thrust generated by the blades was calculated.

3.3 Automated Blade Design

The process of generating the profiles in SolidWorks was then automated using the API to enable rapid production of blade prototypes. This allowed the investigation into the appearance, thickness and integrity of many different aerofoils and twist angles. This enabled blades comprising of several aerofoils to be constructed and how well the aerofoils blend to be assessed. Furthermore it dramatically increased the resolution and accuracy of the blade models. This results in a more perfect blade geometry, and therefore a greater validity of our analysis.

3.4 Prototype Blade Design

For the prototype wind turbine there were a number of manufacturing constraints which limited the scope for blade optimisation. The majority of these were down to the fact the prototypes blades were to be 3D printed, and hence there was a minimum thickness and maximum height that could be printed. Printing also limited the material used to be PLA which is a suitable material but is not the first choice for this application. This resulted in a blade design which does not fully account for tip losses and requires to be a particular thickness for all detail to be printed. Furthermore the printers were not running on high resolution settings to enable more rapid production of prototypes. This increased the thickness required for the blade to be printed reliably.

Blades with multiple profiles were produced however it was concluded the gain in stiffness and strength was outweighed by the losses caused by switching profiles. Appearance is also very important in the design of a micro turbine. Blades with multiple profiles resulted in a unusual joint where the profiles change. In order for this to be avoided multiple similar profiles of varying thicknesses would need to be found or developed and then lofted between. This is outwith the scope of what is possible in this project.

The blades used for the prototype were designed using Eppler 433. This was due to a thickness of 14.2% which is comparatively high and is similar along the full length of the aerofoil and the predictable variation in lift coefficient with respect to the angle of attack. The Eppler 433 was also found to have consistent performance along a large variation in Reynolds numbers, which is well suited to wind turbine applications.
Using the MatLab script in appendix K the blades were then analysed with an angle of attack 3 degrees from stall.

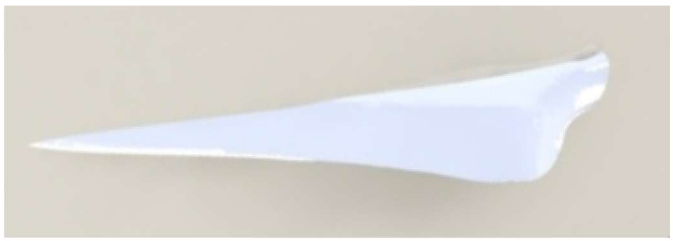

Figure 6: Render of a blade using multiple profiles.

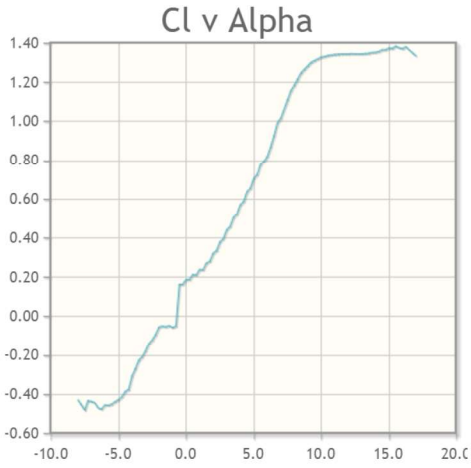

(a) Lift coefficient vs angle of attack

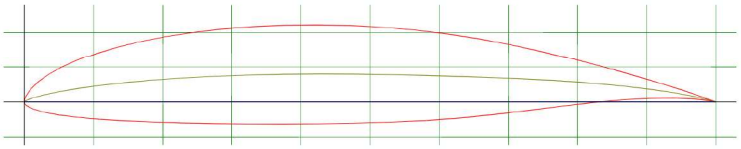

(b) Eppler 433 aerofoil profile

Figure 7

This was to ensure gusts and turbulence don't push the turbine past stall and overload the blade and hub. The blades were analysed for a larger radius and then the top 4 profiles were then removed. This was to ensure the blades were a suitable thickness for printing and would fit inside the printer. This design method greatly increases the tip loss factor and hence reduces the efficiency from the theoretical. In the prototype the blade attachment point was printed separately and was attached using epoxy. These blades were then printed from PLA in the printer and were then tested. This resulted in the blades shown below:

3.5 Final Blade Design

The final blades will be injection moulded from polycarbonate. This is due to it's high strength, impact resistance and the low shrink that occurs when cooling after moulding. This means the moulds can be made to near exact size and no detail will be lost upon cooling. We will use the same aerofoil profile but will be extended to the full extent of the defined shape in MatLab. This is due to the increased resolution possible when injection moulding. They will be 165mm long. The blade attachment point would be incorporated into the mould, resulting in a stronger bond and fewer points of failure.

4 Blade Guard

4.1 Design

The design shown in Figure 8 was chosen as it is simple to manufacture, easily flat-packable, and interferes only minimally with aerodynamic performance of the tail-fin during furling. This assembly (Appendix J Drawing 007)

is made from 2mm and 8mm laser-cut acrylic sections, and has a circular pattern spaced 1200 apart to gain a large arc length for user protection. The base mounts featuring a tapered dove-tail slot, are epoxied onto the nacelle front face, and an M6 threaded rod epoxied to the nacelle runs through a 6mm clearance hole. The guard poles are then slotted into the dove-tail, and a final removable piece is then locked with an M6 nylock nut to limit the pole's final axial degree of freedom. The curved top section of the blade guard involves a similar process, and is fastened with M3 bolts, with stacked washers on each side to avoid cracking the brittle acrylic on tightening.

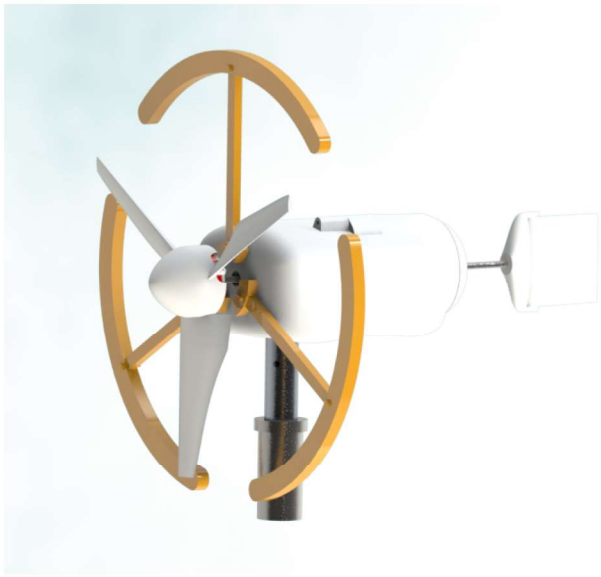

Figure 8: Blade guard assembly for user protection during operation.

4.2 Prototype Development

This design is adjustable, but may still be inconvenient to a hill-walker exposed to the elements as tools are involved. This report therefore proposes the product should be developed with a machined aluminium mount with an M3 thread, the revised poles (made from 3mm Stainless Steel Bar Stock), and curved guards will also have the same corresponding threads to allow for a tool-less disassembly in a compact fashion. This will be suitable for protection of the blades, and user during operation.

5 Hub Assembly

5.1 Design

We decided to adopt a lightweight, modular design for the Hub Assembly, weighing 284.42g. Figure 9 6mm stainless steel shaft of length 125mm that has been turned down on a lathe for 20mm of M4 tapped thread (Appendix J Drawing 002). The hub plates are made from 3mm acrylic laser-cut discs that are bonded together, the complete hub is then secured against the turned shaft with a M4 nylock locking nut. Stacked washers are used between the step, and the nut to prevent the brittle acrylic discs shattering from over-torque.

The hub is composed of two inner disks with blade tab slots sandwiched between two outer disks with pin holes (Appendix J Drawing 003). The blades, and blade tabs were both initially 3D printed from PLA with 10% infill, however a Finite Element Analysis (FEA) study in figure 10 prompted a reprint of the blade tab with 50% infill to deal with localised stress concentrations.
The nose cone (Appendix J Drawing 004) is the final component of the hub assembly, three sections of 6mm stainless steel bar provide a pinned support to slot through the hub disks, and the corresponding blade tab holes, this restricts

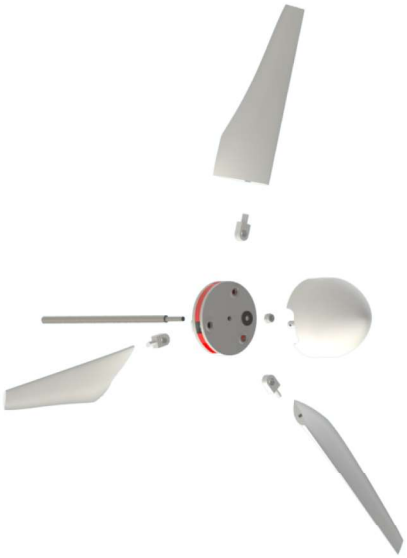

Figure 9: Hub Assembly Exploded View

the blades moving in all degrees of freedom. The stainless steel pins each have a 2mm hole drilled to fit an R-pin made from 1.6mm wire, to limit the movement of the nose cone in the axial direction (figure 9).

Each design choice involved thinking about how the consumer would interact with this assembly in real world conditions, features such as a tool-less disassembly, removable blades for safe storage, and a firm housing for the blade tabs under high rotor speeds are essential. This simple, and modular design helps set YAWT as a market leading product for the outdoor enthusiast.

5.2 Finite Element Analysis (FEA)

We have identified the protruding blade tab, and the nosecone support as two points of weakness in this assembly, simulations were therefore performed using a series of static FEA studies in SolidWorks. The loading conditions were obtained from the MATLAB script (Appendix K) that outputs the integrated thrust force, and torque for the blades using Blade Element Momentum (BEM) theory. The turbine control system actuates the hydraulic shaft brakes using a linear servo motor at 18 m/s wind speed, $20ms^{-1}$ was therefore chosen as the design wind speed for these simulations as a conservative case. This wind speed will generate an axial thrust load of 213.4N perpendicular to the hub and a torque of 0.483Nm. Furthermore, the loading case will also account for a maximum braking torque of 1Nm.

5.3 Blade Tab

This simulation in Figure 10 was set up using a static study in SolidWorks. Firstly, the fixtures were applied, this involved setting each acrylic disk interface as a "fixed contact" to simulate the epoxy joins, the fixtures in the three outer holes were then specified as "pin supports" with a rotational rigidity of $518.74Nmrad^{-1}$ (Appendix F), and finally the four cylindrical hole faces were set to be "fixed geometry".

The thrust load of 213.4N was applied to the outer face of the blade tab, while the torque of 0.483Nm acted on the top face, finally a combined anti-clockwise torque contribution of 1.483Nm from the brakes and the blade was found to act on the outer faces of the acrylic disks.
The blade tab experiences a maximum stress of 34.41MPa during this simulation; the yield strength of PLA is 60MPa [7], this gives the hub a safety factor of 1.75 for these loading conditions. However, as the blade tab was

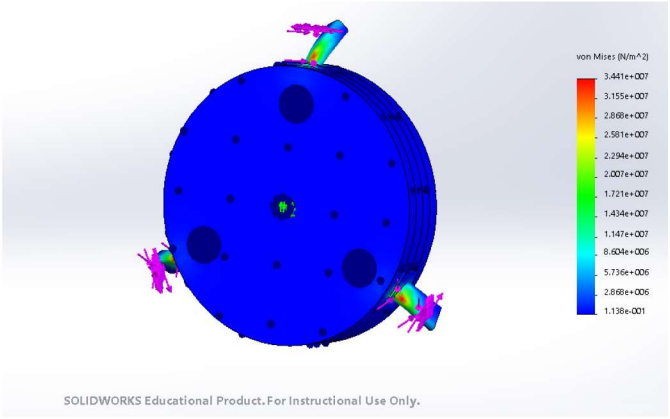

Figure 10: von Mises Stress Plot for Blade Tab and Hub Assembly.

only printed with 50% infill, the yield strength of the part will be lower than the quoted 60MPa (which assumes 100% infill). Following this simulation, the decision was made to increase the fillet radius at the root of the blade tab from 0.5mm to 1mm to reduce stress concentrations. A maximum displacement of 0.22mm occurs at the blade tab tip shown in figure 10, this movement can be negated by the introduction of webbing near the tab.

5.4 Prototype Development

Currently most of the prototype hub assembly is made from acrylic laser cut discs, and 3D printed PLA sections. The assembly also relies on the use of bonded joints on parts such as the hub disks, blade tabs, and nose cone supports. This assembly is therefore a relatively labour-intensive manufacturing process due to the low project budget of £90.00 allocated. Given significant investment, this report would suggest looking to branch into new manufacturing methods that are conducive to mass production with low unit costs. For example, the creation of a durable two-part plastic injection mould will be a large investment with high CNC tooling and coating costs that will amount to approximately £14,234.00 [21] for the physical scale of this project. However, once the mould has been made, the number of parts made an industry standard mould is approximately 5000 [20]. Plastic injection moulding is therefore a cost-effective way to mass produce high quality products with a good geometric accuracy.

6 Drive Train

6.1 Design

The drive-train of the turbine shown in figure x is very compact, spanning 100mm in the axial direction. This assembly consists of two 6mm bore "626-RS Dunlop Sealed Miniature Ball Bearings" (Appendix J Drawing 006) that can rotate up to a speed of 36,000 rpm [9]. The bearings are housed in PLA 3D printed pillow blocks (Appendix J Drawing 006), these mounts feature a counter bored hole in the centre to allow for a face to press-fit the bearings against. The generator assembly (see figure 1a) is found between these bearing mounts to provide stable support for this integral component of the micro turbine. Each of the drive-train components are fastened to a laser-cut 2mm sheet of mild steel using M4 grade 8.8 bolts, with nylock locking nuts.

6.2 Bearing Specification

Figure 12 shows the static loading case for the bearings under radial and axial loading. The front bearing is assumed to provide sole axial resistance, while the radial load bearing comes from the clumped assembly weights. This analysis does not consider rotational torque or inertia loading's, we have neglected the eccentric loading also

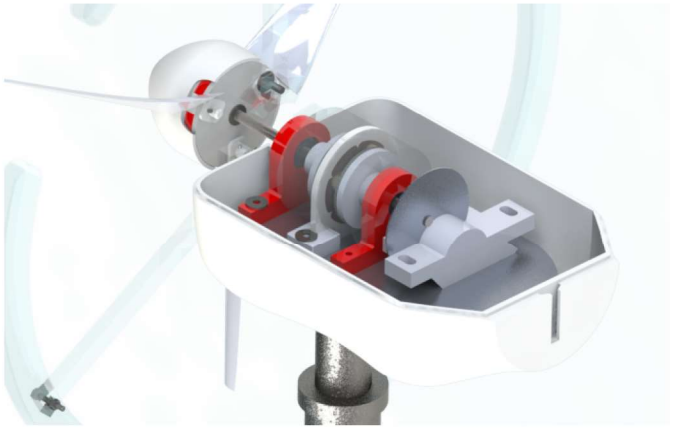

Figure 11: Drive train assembly for YAWT, rendered is situ.

as our analysis proved the deflection of the shaft to be negligible, such that the forces generated by the eccentricity are also considered negligible. The final results of the bearing lifetime analysis (Appendix H) show the bearings

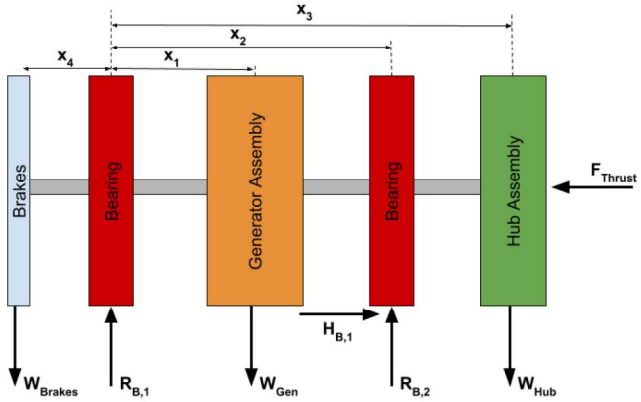

Figure 12: Free body diagram of the drive train assembly bearing arrangement experiencing axial and radial loads.

will last 1696.4 million revolutions, 9424 hours, or 392 days. This report will therefore recommend the producer to not issue warranty in excess of 2 years for this wind turbine.

6.3 Prototype Development

There are two main features that could be revised for the safe, and structurally sound operation of this micro turbine. Firstly, the PLA pillow blocks were printed with an infill of 10%, and a poor print layer height resolution of 300 microns, this resulted in weak mountings that required a strengthening coat of epoxy prior to bearing press fit. A possible improvement be a fully integrated 19mm inner diameter Cast Iron pillow block, although this material displays a high weight with a density of $7800kgm^{-3}$, the bearing does not require a press-fit, as they have a machined groove, and slot system that allows easy assembly, and removal. Secondly, a tapered roller ball bearing may be added to accommodate for high thrust loading cases, especially if the prototype were to scale in size, roller bearings consequently experience less stress due to a line contact between the inner and outer race, rather than a point contact. However, for micro-turbines, a roller bearing is more suitable, as the small contact point generates less friction, and allows a higher operating speed.

7 Brake Design & Control Systems

7.1 Brake Applications

In order to prevent damage to the user or the device, we have implemented an emergency braking system to terminate all motion of the blades, shaft and rotors. There are three scenarios in which this system would be deployed.

The first of these is in high wind speed where the power in the wind is dangerously high, the dump load resistor has reached its capacity and can no longer dissipate the excess power. The furling system has also been deployed to reduce the efficiency of the blades and lower the power input to the generator. Once both of the control measures have been deployed and are still found to be insufficient, the brakes will be applied to terminate all power generation to prevent damage to the moving components and electrical circuits. The trigger for this event is determined by measuring the voltage output from the generator and determining where this point lies with respect to wind speed. The target cut out wind speed is 18m/s and the brakes will be released after 4 hours to test if the wind speed has returned to an operational level. We are looking to implement a manual override in software for the next revision. These conditions are very rare in the UK but can cause severe damage to the turbine E.

The second scenario where the brakes would be applied is in the case of the turbine becoming unstable on the mounting pole or the pole moving in the ground. In this scenario a accelerometer will determine when the turbine has moved from its initial position and the Arduino will use this sensor data to determine when to actuate the brakes.

The third and final situation when the brakes would be applied is when the user opens the nacelle to access the phones. A pressure switch it located between the nacelle and access panel the low output from the switch will cause the Arduino to apply the brakes. This is to ensure no harm is caused to the user when plugging in a phone to charge or checking on their device.

The heat generated from multiple applications in a short period of time has not been considered due to the system only being actuated every few hours, this is assumed to be adequate time to cool. The maximum temperature change experienced by the brake disc when stopping from a wind speed of 20m/s is 28°C. This temperature change from any temperature experienced by the turbine is well within the operating temperatures of all materials within the turbine.

7.2 Braking System

By investigating the torque generated by the blades at 20 m/s, it was found that for the turbine to stop under braking force alone, the brakes would be required to apply more than 0.483Nm of torque. Following this a desired stopping time was chosen. This was to ensure the turbine would come to a halt in a suitable short period of time to limit the potential for harm to the user and damage to the turbine. The period chosen must also be sufficiently long that the torque applied to the hub and drive assembly will not damage any other components. It was decided that a stopping time of 5s was suitable to fulfil all of the criteria. For this reason the brakes are required to produce 0.0573Nm of braking torque. This is equivalent to two brake pads similar in size to those on a bike applying a lateral force of 0.298N at the same radius as the outside of the rotors. This radius was chosen to ensure the device is as compact as possible.

The braking system used for the prototype consists of a re-purposed hydraulic bicycle brake which is actuated by a servo motor. In the prototype the power in the braking system is very limited to reduce the cost and stay within the budget for the prototype.

7.3 Final System Design

For the final system, a pull by wire braking device would be used due to the lower cost, and the ease of production of this system. This would still be actuated by a servo motor. The advantages of a more reliable hydraulic system which has a longer service life with less requirements for maintenance are outweighed by the extra complexity and cost. This extra cost for limited performance difference is further highlighted when the average wind speed in the UK is investigated. It can be seen that the conditions in which the brakes would be applied in high wind speed are very rare and hence the wear on the brakes would be limited.

Figure 13: Cad of final design.

This system will require a higher power to actuate in all wind conditions. For this reason in the final design the electronic circuits will be required to output a higher current to ensure no damage is caused to the control system.

8 Yaw Control Systems

For the reasons discussed previously we have elected to use an upwind horizontal axis turbine configuration. This means we must design a yawing system to orient the blades of the turbine into the wind. Ideally the yawing system should perfectly orient the blades into the wind. Failure to correctly align the blades with the wind direction will cause a lower amount of air to pass through the sweep of the blades. The area presented to the wind varies with the cosine of the angle relative to the direction of the wind.

Given the price point of our turbine active yaw control doesn't make a huge amount of sense as it would require a slewing ring bearing, a dedicated motor, as well as sensory systems to determine the wind direction. Mostly, these systems provide many more potential points of failure, not something that we wish to add to our design. Rather it seems better to compromise on size in exchange for a simpler operation which has a lower probability of failure, and will fail in a usable manner.

8.1 Passive Yaw Control

This system typically involves designing a tail fin that is positioned downwind/behind the blades and nacelle to provide a yawing moment that will align the blades into the wind. This yawing system benefits from a very simple design, and manufacturing process. Such a system relies upon the wind to orient itself. This can be problematic in unstable gusty conditions where there may be a prevalent direction that we wish to orient the turbine towards. However, a tail fin can be too responsive to localised high frequency gusts, this induces potentially large stresses in the turbine blades due to the gyroscopic effects induced by high speed rotation. These stresses are proportional to the angular velocity of yawing, the angular velocity of the blades, and the rotational inertia of the blades [30]. Yaw error will also cause a loss of efficiency that can be approximated using the following equation, where both angles are measured from some arbitrary point.

$$\epsilon = \cos^2(\theta_{turbine} - \theta_{wind})$$

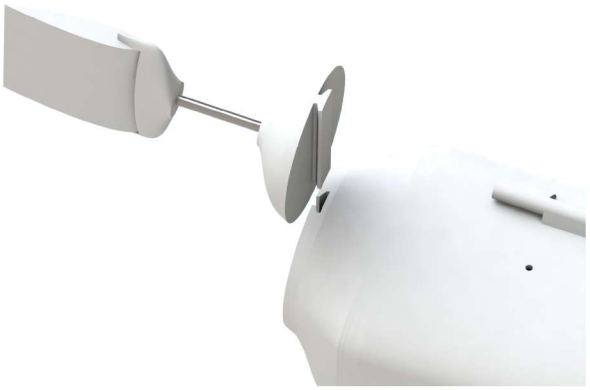

(a) Render showing an exploded view of the tail attachment mechanism.

(b) Image of the cable connector.

Figure 14

Thus we are presented with an optimisation problem of tail size and positioning, in order to yaw the turbine without making it over-responsive to high frequency gusts.

The shape of the tail could be optimised towards a triangular shape which was found to be marginally optimal [22]. However the gains they found seem to be minimal, in addition we wish to include a furling mechanism that incorporates into this design. Rather it is preferable in this situation to aim for a trapezoidal side profile that includes a control surface that will enable us to control the degree of furling, as well as providing passive yaw control when aligned normal to the swept area of the blades.

8.2 Specification for the Yaw Bearing

The yaw bearing needs to provide free movement of the turbine whilst supporting a comparatively large thrust load. Whilst selecting this bearing we will neglect the radial loading, as there is no situation in which this bearing should experience significant angular velocities, the maximum radial loading will be a static load of 213.4N, transferred from the blades. The thrust load it must support is generated by the mass of components plus the mass of the users phone(s), our estimate of mass using two Samsung Galaxy Note 8's is 2.96kg, therefore a force of 29.0376N, taking standard gravity of $9.81ms^{-2}$. The final criteria is that the bearing must have an interior diameter of 30mm in order to clear the mounting post. To this extent we have specified the a Dunlop Deep Groove Ball Bearing 6006-2RS 30mm I.D (see appendix J), this can support a static load of 8.4kN, as well as a thrust load of approximately 4.2kN [9]. This is hugely over specified for our case, however, in this case size was a determining factor. The bearing is sealed to prevent the ingress of particles and liquid, and thereby extend its lifetime. The mass of the final prototype for passive yaw control is 0.201kg, this is mostly distributed towards the nacelle, nevertheless the moment of this component has been considered in locating the yaw bearing under the centre of mass.

8.3 Packing & Toolless assembly

In order to reduce the packed volume of our turbine we elected to make the tail assembly fully detachable, to do so we needed to detach both the assembly as well as the control cable specified for the furling control system. The main assembly detaches via a slotted join shown in figure 14a, the cable connects using a connector shown in figure 14b.

9 Furling

As mentioned in the yawing discussion the volume of air passing through the sweep of the blades varies with the cosine of the angle from the vector of the wind. So furling the turbine out of the wind can be useful to control the power created by the blades, and protect the turbine from damage due to over speed operation. However, the closest edge of the blades to the wind will suffer from a greater bending torque. This is compounded as a problem due to the cyclical loading of the blades as they move from the position closest to the wind, to the opposite position, furthest from the wind and back. This will cause the rapid loading and unloading of the blades, as any attempt to furl will be to maintain the rotational speed at 3000RPM. This could significantly affect the lifetime of the blades by rapidly increasing the cycling of loading on the blades. We will need to conduct an analysis of the expected forces, with respect to the fatigue properties of polylactic acid (PLA), see appendix G [7]. We can see that the thrust forces and torques that we are estimating for our blades could produce a stress that is potentially of concern near the tip. This could be resolved by changing the geometry, or by selecting a more suitable material. PLA will be more than suitable for the purposes of our hardware demonstrator.
Due to the shape of our nacelle and the positioning of the yaw bearing if we choose to furl about the yaw axis then the side profile of the nacelle will cause the turbine to attempt to return to facing into the wind. This same phenomena ties closely to the design of our blade guard

9.1 Active Furling

We considered two means of active furling. Firstly a system using a slew bearing and a stepper motor, we decided against this system for the same reasons as we did when considering this setup for yaw control, though they pair together nicely as a package. The second system uses a control surface in the tail, we opted for this system due to its simplicity, its lower power consumption, and the fact it can still function as yaw control even if the furling mechanism fails. We neglected passive furling as it makes the system sensitive to the centre of mass which is not ideal if the user will affect this by adding a phone of unknown mass and dimensions.

For the control surface we chose to use a symmetrical aerofoil, specifically the NACA 0018 profile. Aerodynamically this should have the desired effect when normal to the plane of the blades because of its symmetrical nature. For low angles of turning we should see minimal separation of flow from the high pressure side of the aerofoil [23]. The choice of material for the prototype was polylactic acid (PLA), however, when exposed to our predicted environments the PLA will begin to degrade. This is unnaceptable to the user and if it fails as suggested in the FMEA (appendix B), would render the turbine nearly non-functional. This report would suggest using polycarbonate (PC), or a polycarbonate, acrylonitrile butadiene styrene (ABS) blend, to match those used in the nacelle. These polymers are far stronger, better suited to mass production techniques like injection moulding, and will not degrade as quickly.

9.1.1 Control Systems

This system will be controlled by a straightforward closed control system. This system will attempt to furl the turbine if the measured voltage frequency exceeds 105Hz ($\approx 3100RPM$). If the frequency exceeds 105Hz the turbine will furl further, if it drops below 100Hz the system will reorient the turbine into the wind. If the turbine wishes to furl beyond 10 deg out of the wind then the micro-controller should trigger the braking system, as wind speed is excessive and furling further will cause the turbine to spin. This system will need to be refined using experimental data.

10 Nacelle

The primary function of the nacelle is to package all of our components in a dust-proof, waterproof environment [19]. This will protect them from the environment and maximise their lifetime. Secondly we have added to the brief that the nacelle should include a means for the user to store their phone, this too will be an IP67 rated

environment, as the user could reasonably expect a safe place to store their device while charging. If the device is larger than the compartment provided a cable can be run out of the enclosure, however this will compromise the IP67 rated enclosure, the product should still meet the standards for an IP54 rated enclosure[6]. This could be adapted with future design to include a third user accessible IP68 rated USB port on the exterior of the nacelle, this would maintain the IP67 enclosure whilst allowing the user to charge outside the enclosure. Alternatively an internal panel could also be made into an IP67 seal creating two seals, the first to protect the turbine components, the second to protect the users device(s).

10.1 Design

10.1.1 Packaging the Components

There are a few key reference points that are unmovable: the yaw bearing housing, the top of the generator, the shaft. The nacelle must accommodate all these features, other points such as mounting points, location of electronics, location of phones are movable constraints. These will be aligned in such a manner to minimise the volume of the turbine, to this end we have made the supporting structure asymmetrical to accommodate the phones along one side of the generator, these are the largest components and must be positioned in the same location as much of the user interface. The final solution showing access to the phones[1] is shown in figure 15a.

(a) Render of the nacelle showing device storage.

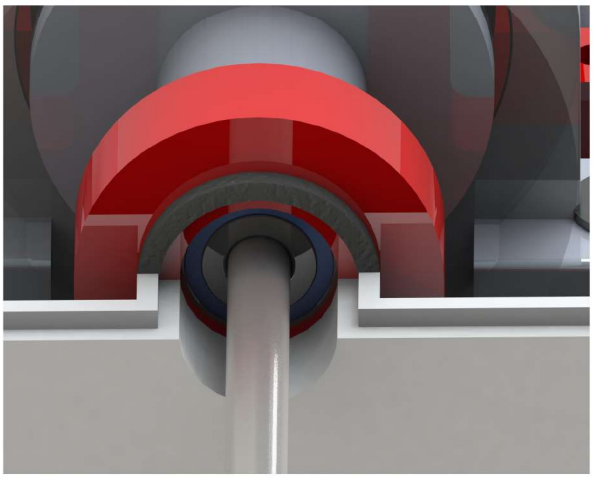

(b) Render of the seal between the nacelle and front bearing housing.

Figure 15

10.1.2 IP67 Rating

The design brief specified a ingress protection level IP67, this means that no ingress of dust can be tolerated, additionally no ingress of water in harmful quantities shall be permitted during temporary submersion. Given the contents of our enclosure contains sensitive electronics as well as the users phone(s), it is assumed that no measurable ingress of water could be considered safe. So where possible any join in the nacelle should use a tongue and groove enclosure, oriented such that the groove faces downward during normal usage. This tolerance was hard to achieve with the prototyping methods available to us, so we have used a lap join here also, as shown in figure 15b. A tongue and groove on this scale created by processes such as injection moulding is at technology readiness level (TRL) 9, as defined by the European Commission (EC) [8]. Where complete separation from the environment cannot be achieved, such as around the drive shaft, we will use seals and gaskets to create a seal around the nearby components. Thereby maintaining the IP67 seal. This strategy was employed using an O-ring seal around the join

[1] Samsung Galaxy Note 8 shown in render.

between the nacelle and the front bearing housing, shown in figure 15b. This seal will be made of a malleable material, this report suggests rubber, or a synthetic alternative, such that the action of assembling the turbine will compress the seal between the nacelle and the front bearing housing and create a watertight, dust-tight seal.

For parts that must be able to move, primarily the access panel, we will use a lap join with a compressible seal. This will allow us the rotational freedom to open the nacelle, whilst still providing surfaces to seal against. The compressible seal ensures that returning the access panel to the closed position will create an acceptable enclosure.

10.2 Analysis

The nacelle will experience some pressure loading from the wind, and some vibration from the rotation of the blades and generator. However, the failure modes and effects analysis (FMEA) conducted in appendix B shows the most probable and severe cause of failure of the nacelle will be from impact, likely from being dropped by the user, or from the mounting post collapsing. To this end the studies we have conducted are to analyse the stresses and strains induced in the nacelle when it experiences such a drop. We set up the drop study in SolidWorks, assuming a drop height of 1m, adding an artificial weight of 1kg to the centroid to represent the internals [25]. The results of our study are shown in figures 16a and 16b. The results of this study show that the stresses at the points of

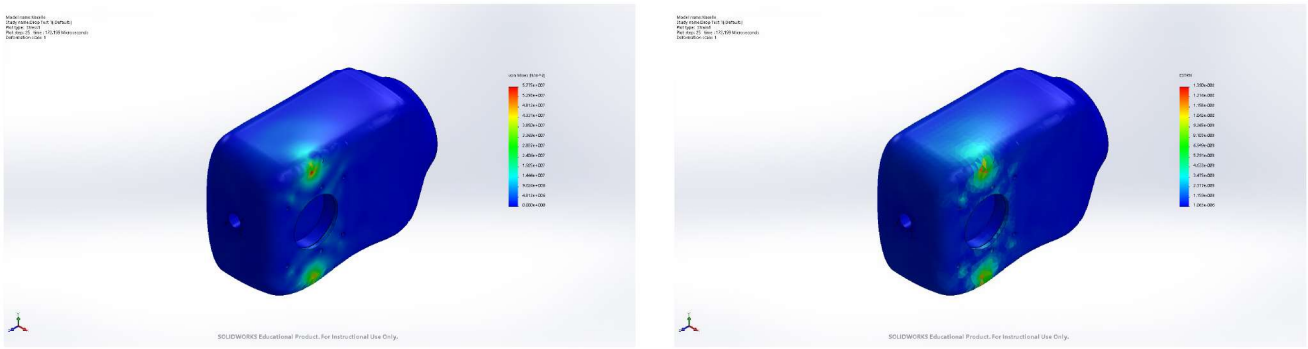

(a) Resulting stress at 172.2μs.

(b) Resulting strain at 172.2μs.

Figure 16: FEA drop study of the nacelle from a height of 1m, including artificial mass of 1kg.

initial contact are dangerously high, this study could be considered conservative as the impacted surface does not yield, but given the propensity of rocks etc. that could apply a point load we believe the concern to be legitimate. Therefore this report will recommend that the material chosen for final production be significantly tougher than the PLA used to prototype, polycarbonate and polyether imide would be valid alternatives.

11 Electronics & Control Systems

11.1 Overview

The design specifications relating to this section include the ability to supply charge to either a single 2.1A or two 1A USB ports. The wind turbine was also requested to begin supplying this charge at an $8ms^{-1}$ wind speed. The electronics control system plays an important role in making this possible whilst assisting in maximising the power output of the turbine. To achieve this the system begins by transforming the 3-phase AC signal from the custom generator to a device compatible DC signal. A series of measurements are taken to determine the turbines current performances forming the bases for intelligent control decisions. To designate which state the system is in required the use of a microcontroller. In this case the Arduino Uno was chosen due to its high level of functionality from its large selections of GPIO pins, and its low power requirement. The system will either decide to reduce or increase the electrical load depending on performance to maximise power and stability of the system. The current will also pass through a charge controller with power path control, which will supply two 1A USBs and 0.5A to power its

own microcontroller simultaneously improving its functionality. The power path control enables the charging and discharging of a rechargeable battery pack on request from the load. The decision to choose a rechargeable battery pack instead of a super capacitor was due batteries being able to store larger amounts of energy for an equivalent size.

11.2 System Design

The first part of the electronic control system is responsible for transforming generated signal into a signal that is compatible with the load and controlling which state the system from monitoring the turbines performance. This section was created in the software package LT SPICE and a diagram is shown in figure 17.

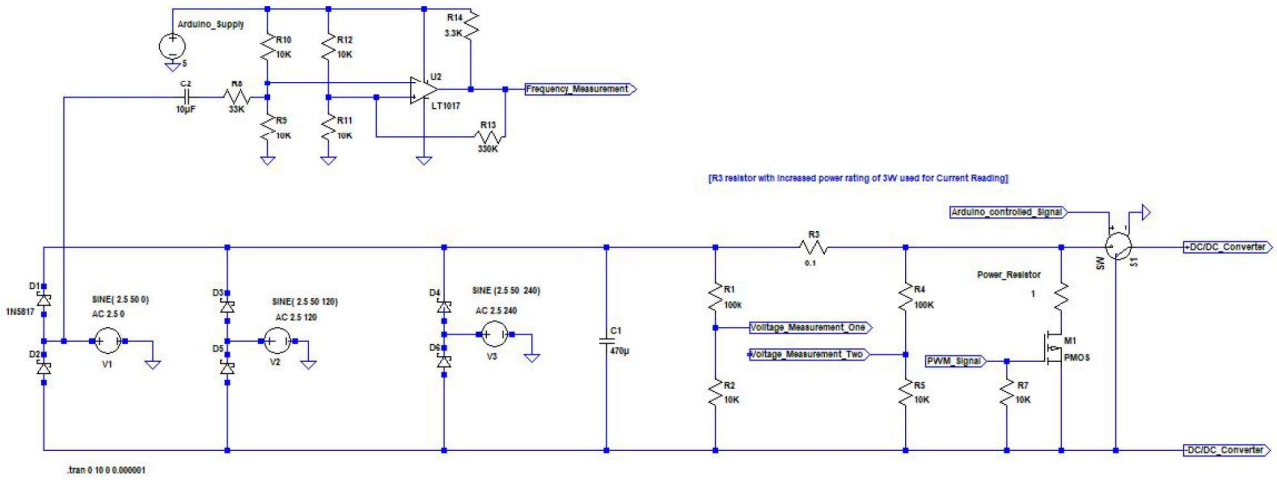

Figure 17: Circuit Diagram of the first section of electronic control circuit.

The first stage is the conversion from of a 3-phase AC signal output from the generator to a DC signal, required for further circuit operation. To achieve this a full wave 3-phase rectifier was constructed using six diodes shown above by D1 to D6. The 1N5817 Schottky diode was selected due to its low voltage drop of 0.45V at the expected 1A per phase from the generator [12]. The low voltage drop characteristic was a key factor in choosing the diode to conserve the realistically lower voltage produced from the generator. The rectifier consisting of three pairs of forward bias diodes that will only allow current to pass through when the voltage it experiences is above its forward voltage. As their input is each a sine wave with 120° phase difference, the result is at any one time the peak positive and negative voltages will allow current to flow up and down through the diodes respectively. This event is continued by different pairs of diodes as different phases reach the peaks voltages. This leads to a potential difference created between the two common lines of the circuit resulting in a DC voltage being received by the rest of the circuit. This DC voltage will have a significant ripple in its waveform causing a degradation in performance of the sensitive components in the circuit. A capacitor was placed in parallel with the rectifier acting as a ripple filter, to stabilise the output by charging and discharging between peaks. The maximum voltage value of the capacitor with a chosen safety factor of 2 of maximum expected voltage required a voltage rating higher than 20V. Additionally due to the expected operating frequency range and the circuit minimum voltage required to operate the DC/DC converter a large capacitance was required. This led to decision to choose an electrolytic capacitor due to their large capacitance and availability. The value chosen of $470\mu F$ is smaller than the size calculated, however, when both were simulated in LT spice there was no significant difference between them. Therefore, the readily available and more compact choice was made. The simulation of the rectifier with the filtered dc ripple is shown in figure 18.
The simulated output from the rectifier above shows a remaining DC ripple at its output. However, this is due to LT spice not performing as intended due to the lack of grounding in the simulated circuit. This will be almost two straight lines near the peaks and the troughs of the output. The important conclusion from this simulation is that the relative voltage between the positive and negative rails is constant resulting in a constant DC value calculated using the output voltage equation presented earlier.

To provide effective control of the turbine the rotor speed was monitored by measuring the frequency of a single

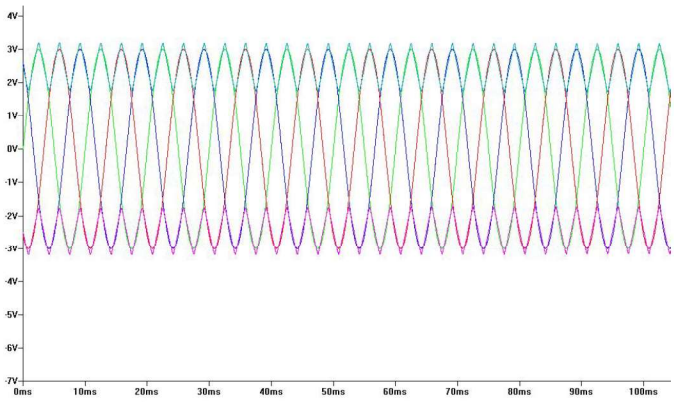

Figure 18: LT Spice simulation of three phase input and filtered DC output.

phase with an Arduino. To achieve this an Integrated circuit (IC) LT1017 shown in figure 17 was used to transform the sine wave to a square wave. This transformation is crucial to measure frequency as the Arduino is unable to measure negative voltage or voltage above +5V. In addition, square wave allows for simpler and memory efficient Arduino coding to measure its frequency. The comparator was selected due to its wide input voltage range which the generator will be supplying and its ability to operate at low currents, important as the Arduino has a limited current supply from its output pins [26]. The comparator and its surrounding circuit changes the waveform by biasing the +V input to 2.5V via the potential divider from 5V supply from the Arduino, and sets the input signal to the input to -V input. If $-V > +V$ input the op-amp equals its output to the negative power supply rail in this case 0V. However, if $+V > -V$ the output is set to the positive rail of 5V. This operation of this comparator is shown in the simulation, figure 19. Figure 19 shows the sinusoidal waveform transformation to the microcontroller

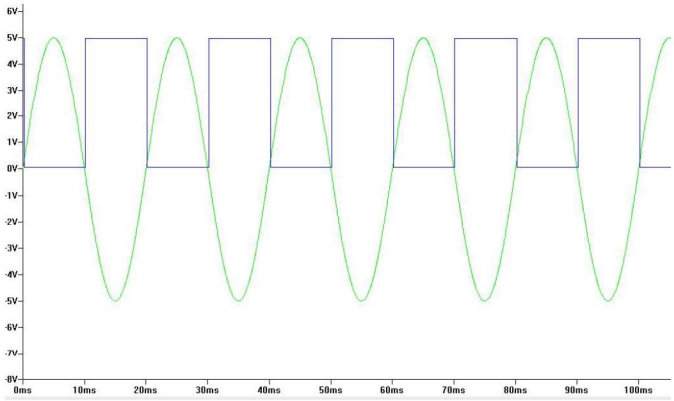

Figure 19: Single phase input vs LT1017 comparator output signal.

compatible square wave enabling the frequency to be measured.

To continually monitor the power being generated a resistor network was designed and is shown in figure 17 of Resistors R1 to R5. This network first measures voltages before and after resistor R3 with a value of 0.1-ohm and 3W power rating using potential dividers. The expected maximum power dissipation through R3 was high enough that it warranted an increased power rated resistor over a traditional resistor with power ratings of only 0.25W. This network first measures voltages before and after R3 with a value of 1-ohm resistance using potential dividers. The potential dividers step down the voltage to safe level between 1-5V for the analogue pins of the Arduino to read. To do this the resistors have a ratio of 10:1 so for example a generated 10V will be measured as 1V. The relatively high values 100K and 10K resistor are chosen to reduce the amount current pulled from the current flowing onto the load. With these two voltages measurements the Arduino can calculate the power output using ohms law and $P = IV$.

To extract maximum power from the turbine the rotor is required to spin at a particular RPM for a certain wind speed, to do this the system requires a variable electrical load. This element of control is achieved by the inclusion

of a power N channel MOSFET and a Power resistor, shown in figure 17. The selected MOSFET has a low gate threshold voltage of approximately 3V and a high current rating making it suitable to be can activated by an Arduino output pin, whilst easily handling the expected current of 3A [5]. The dump load of which the MOSFET controls the flow power to, is the HS25 25W power resistor. This resistor can dissipate the maximum power expected with a safety factor of 1.6. This does require mounting to a heat sink to remain in a in a safe temperature range[27]. In this case the power resistor is mounted to the turbines steel base plate for heat dissipation. The MOSFET is controlled using the Arduino pulse wave modulation (PWM) digital output pin which can be figured to choose how much current the MOSFET allows to flow to the dump load. Furthermore, another component in added to improve the performance of the turbine which is an electrical relay shown figure 1 as S1. This is rated at 10A 20V voltage and is a switch controlled by a digital output pin allowing the disconnecting between the generator and the USBs electrical load. The relay was selected due to its high-power rating and for its ease of use resulting in a highly reliable switch.

The Arduino makes the decision of which state to have the MOSFET and relay in based on the state of the turbine from its power and frequency measurements. The necessary code written to operate this system effectively is still under development and with further testing the system will by optimised. However, an example of the of the type of control to expect is given. If the power. If the power output remains constant and the frequency and therefore rotor speed increases by 20%, meaning the rotor is nearing a situation where its spinning out of control due to lack of electrical load. In this case the PWM signal is frequency is increased on the MOSFET gate to increase the load the power resistor puts on the turbine and an RPM to wind speed balance is reinstated. Conversely if the rotor speed decreases along with the power then the PWM signal frequency would be reduced to lessen the load on the system and help the speed of the rotor recover. The relay is normally connected to the load, however if the frequency is measured to be below 10Hz the relay is switched and the electrical load is disconnected helping the generator back up to operating speed, returning the relay back to its original position.

The second part of the control circuit includes the battery and load management side of the control system. This section receives the set voltage of 8.5V from the DC/DC converter and powers the charge controller IC and the load. The charge controller and its surrounding circuitry is designed to provide safe charging to the battery pack whilst ensuring the load is being supplied at every potential moment. The charge controller selected for this application in the LTC 4060[27] which allows for highly customisable management system and for rapid charging of the battery. The controller is programmed via the chosen external components and its circuit is shown in figure 20. The circuit

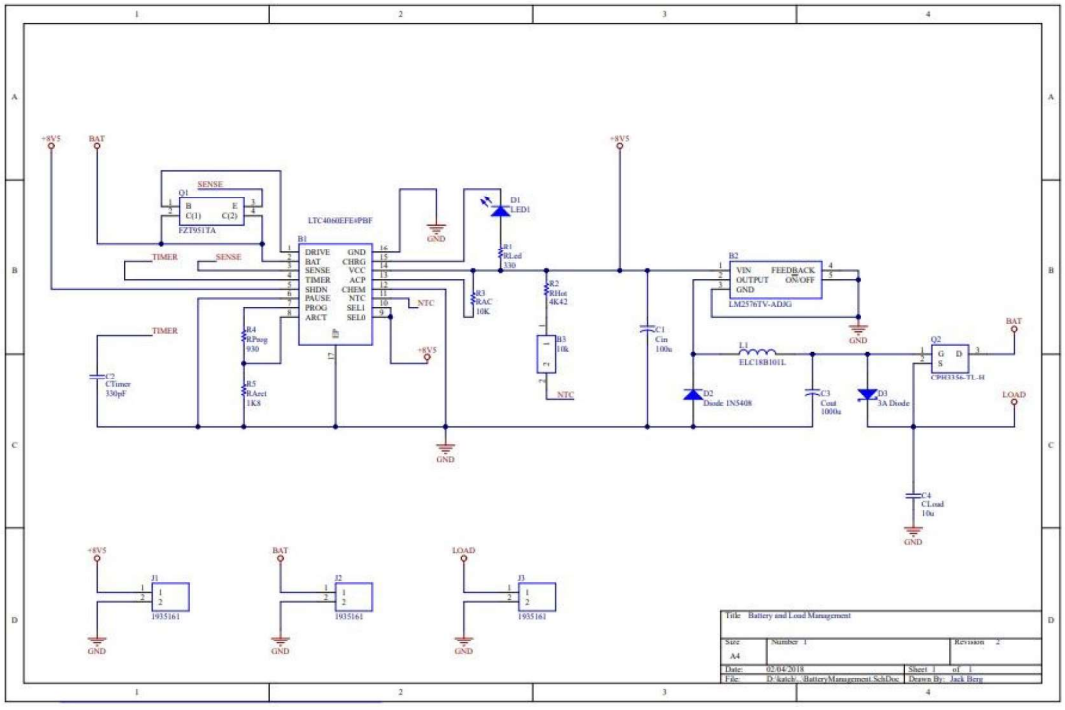

Figure 20: Control system charge controller circuit diagram.

in figure 20 shows the IC charge controller that's prime function is to the control the battery charging. The current will arrive at V_{cc} pin 14 acting as the input power for the charge controller. In this case the labelled CHRG pin 15 will pull it to ground when voltage at V_{cc} > lock out voltage of 8.3V when charging four cells, powering the LED indicating charging has commenced. The potential divider connected to pins 7 and 8 programs the charging rate. This was designed to operate at 0.5A by selecting resistor R_{PROG} and R_{ARCT} values to 930 and 1.8K ohms respectively. This decision was made to allow for the fastest possible charging whilst still not exceeding realistic current available. The capacitor on pin 4 sets the maximum charge cycle times, which with the chosen a 340nF capacitor sets the time to 1.5 hours with an estimated a battery sampling rate of 30 seconds. This capacitor value is selected to ensure the battery is not being dangerously overcharged. To further monitor the performance of the battery the IC pin 11 NTC programs the temperature at which the charging will cease preventing from damaging the batteries. The resistor selected to measure the battery temperature is a standard 10K NTC thermistor which is placed at the edge of the PCB as close as possible to the battery to accurately monitor its temperature. The resistor placed in series with the thermistor sets the maximum temperature as when the resistors equal in value charging is terminated. In inspecting the battery datasheet its upper limit for safe operation is at the of temperature of 50°, therefore using the thermistor datasheet [10]and finding its resistance at said temperature R_{HOT} is selected to be 3.4K ohm. The transistor shown in the diagram as Q1 is responsible to pass the current from the V_{cc} pin through its emitter to its collector initiated from its base from the Drive pin, to charge the battery. The transistor selected for this was a BJT PNP transistor which could pass the maximum charge current of 2A to allow for future tuning of the charging rate.

These settings all contribute to how the charge controller mangers the charge sent to the battery pack via the pin named B_{at}. The battery pack that was selected for this design contains four AA sized ANSMANN 2950mAH NIMH cells in series [3]. These cells where selected due to their high discharge rate of 5A and max voltage of 1.5V. These values are crucial as the potential draw from the battery could be as high as 3A and the load is expecting a voltage between 7 to 4V. The decision to specifically use NIMH batteries is due to their high discharge rate at a low price point making them superior over the alternative charger controller compatible NICd cells.

To maximise the time the load can be successfully supplied there is a power path control system also included in the circuit shown in the diagram above. When there is sufficient power being generated the 8.5V at V_{cc} will be step down to 5v volts via the switching regulator labelled as B2, and pass through the Schottky diode to the load. The voltage regulator chosen was the LM2576[15] due to its high current rating of 3A which it is expected to pass when fully operational and with its adjustable voltage output settings. In this case the voltage regulator is set to output 5V with its surrounding circuitry. The stepping down of the voltage is an important conversion as the USB load requires a voltage lower than the 8.5V needed to charge the 4-cell battery pack. In the event where there is insufficient power being generated to supply the load the P channel MOSFET labelled as Q2 turns on enabling the battery to discharge from its drain to its source supplying the load. The MOSFET selected was the DMP2170U[13] due to its ability to pass the expected 3A with a higher efficiency that alternative PNP BJT Transistor. This battery and load control circuit is manufactured onto a custom designed PCB which is shown in the appendix C.

11.3 Future System Improvements

The first stage of the control circuit is currently soldered onto a perforated board, to improve production scalability and size this should transferred to a PCB. The used microcontroller of the Arduino Uno although providing a strong prototyping platform is under utilised in this application making it inefficient choice for a production product. In this case an ASIC board should be developed so that the processing required by the system can be done as efficiently as possible saving on power and space. Currently the code decides the state based on a range of values it reads on the performance and lacks accuracy when trying to keep the RPM at its optimum for a given wind speed. To improve this the current exact readings should be mapped to corresponding microcontroller output values that accurately decide the turbines power and RPM to the optimum settings.

References

[1] M. A. Almozayen, M. K. El-Nemr, and E. M. Rashad. "Design procedure of coreless stator PM axial field synchronous machine for small-scale wind applications". In: *Electrical Engineering* (May 2017). ISSN: 1432-0487. DOI: 10.1007/s00202-017-0540-4. URL: https://doi.org/10.1007/s00202-017-0540-4.

[2] American National Standards Institute (ANSI). *ISO 1222:2010, Photography - Tripod connections*. 2010.

[3] Ansmann. *Datasheet: AA - 2500mAh low self discharge 2pcs blister package*. July 2016. URL: https://docs-emea.rs-online.com/webdocs/1502/0900766b815029c4.pdf.

[4] H. Arabian-Hoseynabadi, H. Oraee, and P.J. Tavner. "Failure Modes and Effects Analysis (FMEA) for wind turbines". In: *International Journal of Electrical Power Energy Systems* 32.7 (2010), pp. 817–824. ISSN: 0142-0615. DOI: https://doi.org/10.1016/j.ijepes.2010.01.019. URL: http://www.sciencedirect.com/science/article/pii/S0142061510000281.

[5] Arcol. *Datasheet: HS Aluminium Housed Resistors*. Apr. 2017. URL: https://docs-emea.rs-online.com/webdocs/15a2/0900766b815a2308.pdf.

[6] Thc Elcctrical Installation Equipmcnt Manufacturers' Association. *Guide to the IP Codes for Enclosures, Degree of Protection BS EN 60529: 1992 (IEC 529 1989)*. 2001.

[7] Rodney D. Averett et al. "The mechanical behavior of poly(lactic acid) unreinforced and nanocomposite films subjected to monotonic and fatigue loading conditions". In: *Journal of Composite Materials* 45.26 (2011), pp. 2717–2726. DOI: 10.1177/0021998311410464. eprint: https://doi.org/10.1177/0021998311410464. URL: https://doi.org/10.1177/0021998311410464.

[8] European Commission. *COMMISSION IMPLEMENTING DECISION of 22.7.2014 amending Implementing Decision C(2013)8631 adopting the 2014-2015 work programme in the framework of the Specific Programme Implementing Horizon 2020 – The Framework Programme for Research and Innovation (2014-2020)*. 2014, Chapter 19.

[9] Dunlop. *Dunlop Bearing Catalogue: Ball, Tapered, and Roller Bearings*. 2017.

[10] Epcos. *NTC thermistors for temperature measurement Leaded NTC thermistors, lead spacing 5mm*. Apr. 2010. URL: https://produktinfo.conrad.com/datenblaetter/500000-524999/500622-da-01-en-Heissleiter_B57164_K164_10K_5Prozent.pdf.

[11] NILS FERBER. *Micro Wind Turbine*. http://nilsferber.de/#/micro-wind-turbine/.

[12] Diodes Incorporated. *Datasheet: 1N5817 - 1N5819, 1.0A SCHOTTKY BARRIER RECTIFIER*. Aug. 2015. URL: https://www.diodes.com/assets/Datasheets/ds23001.pdf.

[13] Diodes Incorporated. *Datasheet: DMP2170U 20V P-CHANNEL ENHANCEMENT MODE MOSFET*. 2016. URL: https://www.diodes.com/assets/Datasheets/DMP2170U.pdf.

[14] British Standards Institute. *BS EN 60529:1992+A2:2013, Degrees of protection provided by enclosures (IP code)*. 1992.

[15] Texas Instruments. *LM2576xx Series SIMPLE SWITCHER® 3-A Step-Down Voltage Regulator*. 2018. URL: http://www.ti.com/lit/ds/symlink/lm2576.pdf.

[16] C.W.T. McLyman. *Transformer and Inductor Design Handbook, Fourth Edition*. CRC Press, 2017. ISBN: 9781315217666. URL: https://books.google.co.uk/books?id=yOXRswEACAAJ.

[17] Biadgo Asress Mulugeta and Aynekulu Gerawork. "Aerodynamic design of horizontal axis wind turbine blades". In: *FME Transactions* 45.4 (2017), pp. 647–660.

[18] Met Office. *Renewable energy investment*. 2016. URL: https://www.metoffice.gov.uk/services/industry/financial/renewables-investment.

[19] OSRAM. *Technical application guide IP codes in accordance with IEC 60529*. 2012.

[20] Rex Plastics. *How Much Do Injection Molds Cost?* 2013. URL: https://rexplastics.com/plastic-injection-molds/how-much-do-plastic-injection-molds-cost.

[21] Protolabs. *Injection Moulding Design Tip — 9 Ways To Reduce Costs*. 2018. URL: https://www.protolabs.co.uk/resources/design-tips/9-tips-to-reduce-injection-moulding-costs/.

[22] Nikhil Raikar and Sandip Kale. “Effect of Tail Shapes on Yawing Performance of Micro Wind Turbine”. In: 4 (Jan. 2015), pp. 38–42.

[23] Mohammad H Sadraey. *Aircraft design: A systems approach to engineering*. Wiley, 2013.

[24] SKF. 2018. URL: http://www.skf.com/in/products/bearings-units-housings/super-precision-bearings/angular-contact-thrust-ball-bearings-for-screw-drives/equivalentbearingloads/index.html.

[25] Dassault Systemes. *White Paper: Simulating Drop Tests in SolidWorks*. 2009. URL: https://www.solidworks.com/sw/design-validation-whitepapers.htm.

[26] Linear Technology. *Datasheet: LT1017/LT1018 Micropower Dual Comparator*. Mar. 2018. URL: http://www.analog.com/media/en/technical-documentation/data-sheets/10178ff.pdf.

[27] Linear Technology. *Datasheet: LTC4060 Standalone Linear NiMH/NiCd Fast Battery Charger*. Mar. 2018. URL: http://www.analog.com/media/en/technical-documentation/data-sheets/4060f.pdf.

[28] Engineering Toolbox. 2018. URL: https://www.engineeringtoolbox.com/modulus-rigidity-d_946.html.

[29] WaterLily. *WaterLily Wind and Water Turbine*. 2018. URL: https://waterlilyturbine.com.

[30] David Wood. “Small Wind Turbines”. In: *Advances in Wind Energy Conversion Technology*. Ed. by Mathew Sathyajith and Geeta Susan Philip. Berlin, Heidelberg: Springer Berlin Heidelberg, 2011, pp. 195–211. ISBN: 978-3-540-88258-9. DOI: 10.1007/978-3-540-88258-9_8. URL: https://doi.org/10.1007/978-3-540-88258-9_8.